



# Direct unassisted hydrogen peroxide generation from oxygen and water on plasmonic Ag-graphene-Cu nanosandwich

Yaxing Liu<sup>a,c</sup>, Fuyi Chen<sup>a,b,c,\*</sup>, Qiao Wang<sup>a,b</sup>, Junpeng Wang<sup>a,b</sup>, Jiali Wang<sup>a,b</sup>

<sup>a</sup> State Key Laboratory of Solidification Processing, Northwestern Polytechnical University, Xi'an 710072, China

<sup>b</sup> School of Materials Science and Engineering, Northwestern Polytechnical University, Xi'an 710072, China

<sup>c</sup> School of Electronics and Information, Northwestern Polytechnical University, Xi'an 710072, China

## ARTICLE INFO

### Keywords:

Plasmonic nanostructure

Hot-electrons

Photocatalytic oxygen reduction reaction

Hydrogen peroxide

## ABSTRACT

A nanosandwich made from Ag nanoparticles (Ag NPs) arrays, the two-dimension single-layer graphene (SG) and metallic Cu contact was constructed for the hydrogen peroxide (H<sub>2</sub>O<sub>2</sub>) generation utilizing solar energy without an external bias. The shifting of binding energy towards lower energy in Ag core-level electronic spectrum is an evidence of strong coupling between Ag and graphene, which can efficiently transfer hot-holes from Ag to Cu by a built-in electric field so that the hot-electrons on Ag NPs are directly utilized to initiate the H<sub>2</sub>O<sub>2</sub> generation. This Ag-graphene-Cu nanosandwich can provide a stable photocurrent of  $-15.8 \mu\text{A cm}^{-2}$ , a stable photovoltaic voltage of  $17.5 \text{ mV cm}^{-2}$ , and a H<sub>2</sub>O<sub>2</sub> yield of  $229.33 \mu\text{M}$  after 6 h. To understand the mechanism of oxygen reduction reaction (ORR) in Ag-graphene-Cu systems, the electron transfer number for photocatalytic ORR and the surface facet of Ag NPs were studied. The Ag NPs in Ag-graphene-Cu systems with the deposition time of 180 s clearly shows that an amount of <200> facets are distributed on Ag nanoparticle surface, which can catalyze ORR by 2-electron pathway to generate H<sub>2</sub>O<sub>2</sub> efficiently. This novel Ag-graphene-Cu nanosandwich offers a new transfer path for hot-electrons and potentially provides a new concept for driving efficient solar energy to chemical energy.

## 1. Introduction

Solar energy is an attractive candidate for alternative energy because it is the most abundant and sustainable natural energy source. Each year, the Earth receives solar energy at a rate of  $\sim 120\,000 \text{ TW}$ , which is 104 times higher than the current global energy demand. A solar cell can convert solar energy into electricity for direct use or storage in batteries. Direct conversion of sunlight into fuels, often termed solar fuels, involves converting solar energy into chemical energy with the aid of an artificial photocatalyst. Solar fuels are an attractive solution for sustainable energy because they can store the photon energy at a high density and for long-duration [1]. Current solar fuels primarily take the form of hydrogen (H<sub>2</sub>) which is generated with solar driven water splitting and are regarded as a low mass and high energy carrier. However, the low efficiency of solar hydrogen production and the storage problem of gaseous H<sub>2</sub> remain one of the greatest obstacles to the large-scale commercialization of hydrogen fuel cells [2,3]. As an alternative solar fuel, the hydrogen peroxide (H<sub>2</sub>O<sub>2</sub>) is a hydrogen storage medium and energy storage chemical for hydrogen peroxide fuel cell, which can produce electricity with only water as a

byproduct, and possess an advantage of its easy storage and safe operation [4]. Moreover, H<sub>2</sub>O<sub>2</sub> itself is a key oxidizing agent for green and sustainable chemistry, which can be used for the paper industry and water treatment. The commercial H<sub>2</sub>O<sub>2</sub> is commonly produced by the anthraquinone method requiring the direct reaction between the hydrogen and oxygen gas on Pd-based catalysts [5–7]. The manufacturing process is not environmentally benign and has a danger of hydrogen gas explosion.

Photocatalytic generation of H<sub>2</sub>O<sub>2</sub> from water and oxygen utilizing solar energy is an eco-friendly, safe, and economical method [8,9]. Traditionally, various TiO<sub>2</sub>-based photocatalysts have been developed for the photocatalytic H<sub>2</sub>O<sub>2</sub> generation, where the photoexcited hot electrons are utilized to initiate oxygen reduction reactions (ORR) on or near the semiconductor surface [10–12]. For example, the TiO<sub>2</sub> with surface passivation by fluoride has produced the H<sub>2</sub>O<sub>2</sub> with steady state concentration levels up to  $1.3 \text{ mM}$  under UV irradiation in the presence of a hole scavenger [13]. The reduced graphene oxide-TiO<sub>2</sub> hybrid catalyst has enhanced the solar generation of H<sub>2</sub>O<sub>2</sub> up to  $4.5 \text{ mM}$  with the presence of phosphate on the TiO<sub>2</sub> surface [14]. However, weak interaction of incident light with these conventional photocatalysts

\* Corresponding author at: 127 West Youyi Road Xi'an Shaanxi, 710072 PR China.  
E-mail address: [fuyichen@nwpu.edu.cn](mailto:fuyichen@nwpu.edu.cn) (F. Chen).

hinders the further performance improvement. Therefore, binary nanoparticles consisting of a plasmonic metal and a semiconductor seem more promising for producing solar fuels including  $\text{H}_2\text{O}_2$  field.

The plasmonic metals, such as Au, Ag, Cu, Al [15], and Bi [16], can improve the semiconductor-based photocatalysis in the entire visible light wavelength region based on the surface plasmon resonance (SPR) effect [17–19]. On photoexcitation from the noble metal nanostructures under light irradiation, SPR can decay and transfer the energy identical to that of incident photons into the conduction-band of metals, generating a great number of plasmonic hot-electrons, similar to the photoexcited hot electrons on the  $\text{TiO}_2$  surface [20,21]. The plasmonic hot-electrons show the great potential for enhancing surface reactions by strengthening interactions with light and reactant molecules, and have been widely utilized in the catalytic redox reaction by providing either electron or energy [22,23]. Recently, Au nanoparticles loaded on the  $\text{TiO}_2$  photocatalysts were investigated to generate  $\text{H}_2\text{O}_2$ , which achieved a high  $\text{H}_2\text{O}_2$  concentration level of 14 mM [24]. Furthermore, Qian et al. [25] investigated the  $\text{H}_2$  production from water reduction in Au- $\text{TiO}_2$  heterostructures under two different visible light ranges ( $\lambda > 400$  nm and  $\lambda > 435$  nm). They demonstrated that the observed  $\text{H}_2$  production from large Au- $\text{TiO}_2$  under  $\lambda > 435$  nm irradiation can only be attributed to SPR-mediated electron transfer from the Au NPs to the  $\text{TiO}_2$  support, the large potential energy of hot electrons induces a fast and efficient transfer into the conduction-band of  $\text{TiO}_2$  under  $\lambda > 435$  nm excitation. Kobayashi et al. [26] reported the photocatalytic ORR activities of Au/ $\text{TiO}_2$  and Pt/ $\text{TiO}_2$  in an aerated aqueous solution containing 4% ethanol. They demonstrated that the initial rate of  $\text{H}_2\text{O}_2$  generation in the Au/ $\text{TiO}_2$  system was much greater than that in the Pt/ $\text{TiO}_2$  system, Au nanoparticles could provide active sites to catalyze the 2-electron ORR to  $\text{H}_2\text{O}_2$ , whereas Pt catalysed the 4-electron ORR to  $\text{H}_2\text{O}$ . Guo et al. [27] demonstrated that the developed Au- $\text{TiO}_2$  plasmonic films exhibited significantly enhanced ORR catalytic activities with an onset potential of 0.92 V (vs. reversible hydrogen electrode), electron transfer number of 3.94, and limiting current density of  $5.2 \text{ mA cm}^{-2}$ . Wen et al. [28] reported that the Ag/AgCl- $\text{CeO}_2$  hybrid composite catalyst exhibited enhanced photocatalytic activity for the photodegradation of norfloxacin (NOF) under visible light irradiation. The hot-electrons generation from the effective separation of photoinduced charge in Ag/AgCl- $\text{CeO}_2$  hybrid composites can be used to enhance the composites effective mineralization ability toward the NOF molecule degradation. Silva et al. [29] reported that, upon visible light irradiation on the Au nanoparticles of the Au- $\text{TiO}_2$  photocatalyst, hot electrons from Au were injected into the conduction band of  $\text{TiO}_2$ , which led to the generation of holes in the Au nanoparticles and electrons in the  $\text{TiO}_2$ . The  $\text{H}_2$  was generated on  $\text{TiO}_2$  and the  $\text{O}_2$  was generated on Au nanoparticles when sacrificial electron donor or acceptors were involved in the solution.

As in the case of natural photosynthetic systems, the binary plasmonic metal and semiconductor hybrid catalyst involves a light harvesting system and a co-attached electrocatalyst. The plasmonic metal works as a light harvesting agent, which captures and converts hot electrons into the redox potentials required for driving the oxygen reduction reaction [30]. The semiconductor like  $\text{TiO}_2$  meets the requirements as electrocatalysts, which are able to catalyze desired reactions ( $\text{O}_2 + \text{H}_2\text{O} + 2\text{e} = \text{H}_2\text{O}_2$ ) with relatively low overvoltage. Unfortunately, the application of hot-electrons in the plasmonic metal and semiconductor hybrid catalyst for redox reaction is limited by the transfer processing, that is, the hot-electrons generated from the plasmonic nanoparticles are required transfer to the catalytic nanoparticles where the reduction or oxidation reaction occurs [31–34]. This prolonged transport path of hot-electrons not only promotes unwanted reverse reactions (recombining the hot-electrons and photon), but also leads to the energy-loss of hot-electrons that seriously reduces the efficiency of photocatalytic reactions. In practice, the plasmonic Au, Ag, and Cu nanoparticles can serve as both the light harvester [21,24] to produce the hot electrons and the electrocatalyst [22,23] to provide the

catalytically active surface for a redox reaction. However, the hot-electrons generated by these direct plasmonic catalysts have not been directly exploited to promote catalytic reactions in previously reported binary plasmonic metal and semiconductor hybrid catalyst systems.

Herein, a new transfer pathway of the hot-electrons generated on Ag nanoparticles is designed so that the hot-electrons can directly be exploited to induce the generation of  $\text{H}_2\text{O}_2$  on plasmonic nanosandwich of Ag-graphene-Cu. In the nanosandwich structure, a layer of Ag nanoparticles was loaded on a two-dimensional large-area single-layer graphene with Cu contacts, the nanosandwich will be denoted as Ag NP/SG/Cu for short here in later. Upon photoexcitation of Ag nanoparticles, the hot holes from Ag nanoparticles can efficiently be transferred to Cu contacts by an electric-field built in the Ag NP/SG/Cu nanosandwich electrode, so the hot-electrons on Ag nanoparticles are directly utilized to initiate the  $\text{H}_2\text{O}_2$  generation without an applied external bias. This Ag NP/SG/Cu nanosandwich electrode system can provide a stable photocurrent of  $-15.8 \mu\text{A cm}^{-2}$ , a stable photovoltaic voltage of  $17.5 \text{ mV cm}^{-2}$ , and a yield of  $\text{H}_2\text{O}_2$  of  $229.33 \mu\text{M}$  after 6 h in an oxygen saturated aqueous solution under simulated solar illumination with the ethanol as electron donor to the oxidation counter-reaction. This conceptually important work provides exciting new opportunities for driving efficient solar energy to chemical energy conversion process by plasmon in a photocatalytic  $\text{H}_2\text{O}_2$  generation system under solar light irradiation without a bias.

## 2. Experimental and method

### 2.1. Fabrication of Ag NP/SG/Cu nanosandwich electrode

Ag nanoparticles were deposited on unheated graphene on Cu foil substrate using a home-built ion-sputtering system. The vacuum chamber had a diameter of 11.5 cm and a height of 13 cm. Metallic silver with purity of 99.999% and a diameter of 5.8 cm was used as a sputtering target. The base pressure of the deposition chamber was about  $6.5 \times 10^{-2}$  mbar. Ultra-high purity Ar (99.999%) was used as a sputtering gas. The pressure of Ar was kept at a constant value of 66.64 mbar. The distance between target and substrate was around 5 cm. The discharge was generated by a DC power supply. The working voltage was kept at 1 KV. The working current was kept at 5 mA. The working time was set as 120 s. Single-layer graphene grown on the Cu foil was purchased from Vigon Technologies Co., Ltd.

### 2.2. Physical characterization

The morphology and structure of the as-prepared samples were observed by field emission scanning electron microscope (FE-SEM; JSM-7500F) and atomic force microscopy (AFM, Bruker's Dimension Icon) in tapping mode. The crystal structure was characterized using the X-ray diffraction (XRD; D/max-2500) with Cu K $\alpha$  radiation ( $\lambda = 1.5406 \text{ \AA}$ ). The accelerating voltage and current employed were 40 KV and 40 mA, respectively. X-ray photoelectron spectroscopy (XPS) characterization was performed on an ESCA Lab 250 instrument under ultrahigh vacuum ( $10^{-9}$  Torr) using monochromated Al K $\alpha$  radiation ( $h\nu = 1486.6 \text{ eV}$ ) to examine the surface composition and electronic structure, all the binding energy were calibrated by the carbon peak (C1s) at about 284.5 eV.

### 2.3. Electrochemical and photoelectronic measurements

All electrochemical (i.e., rotating disk electrode (RDE) polarization and electrochemical impedance spectroscopy (EIS) curves) and photoelectronic (i.e., amperometric i-t, and open circuit potential-time (v-t) polarization, and limiting current density curves) properties were studied at room temperature. The experiments were performed on a CHI660C electrochemical workstation (Chenhua Instrument, Shanghai). A classic three electrode cell, containing a RHE electrode, Pt

electrode, and the as-prepared samples as the reference, counter, and working electrode, respectively. The photo-irradiation effect on the electrochemical characteristics was investigated under simulated solar illumination (AM 1.5 G, 100 mW cm<sup>-2</sup>, wavelength, 295–2000 nm). The ORR activities were studied via measuring rotating disk electrode (RDE) polarization curves. The potential range was from 1.05 to 0.05 V at a scanning rate of 10 mV s<sup>-1</sup>. The rotation rates were controlled at 100, 400, 800, and 1600 rpm. The electrolyte was 0.1 M KOH solution. The Koutecky-Levich (K-L) equation was used for the calculation of the *n* value, as follows [35]:

$$J^{-1} = J_k^{-1} + (0.62nFCD^{2/3}\nu^{-1/6}\omega^{1/2})^{-1} \quad (1)$$

Where, *J* is the measured current density, *J<sub>k</sub>* is the kinetic current density of the ORR,  $\omega$  is the angular velocity of the disk, *n* is the overall number of electrons transferred during the oxygen reduction, *F* is the Faraday constant (96485C mol<sup>-1</sup>), *C* is the bulk concentration of O<sub>2</sub> (1.2 × 10<sup>-3</sup> mol cm<sup>-3</sup>), *D* is the diffusion coefficient of O<sub>2</sub> (1.9 × 10<sup>-5</sup> cm<sup>2</sup> s<sup>-1</sup>), and  $\nu$  is the kinetic viscosity of the electrolyte (1.1 × 10<sup>-2</sup> cm<sup>2</sup> s<sup>-1</sup>). To qualify the ORR process on this novel nanosandwich structure, the K-L plots were obtained for each sample at 0.2 V vs. RHE on the LSVs at various rotating speeds.

The EIS characters were studied in 0.1 M KOH solution at a bias of 0.57 V (vs RHE) in the frequency range of 0.1 Hz to 10 kHz. The Butler-Volmer equation was used for the calculation of the charge transfer resistance (*R<sub>CT</sub>*), as follows [36,37]:

$$R_{CT} = \frac{RT}{i_0 n F} \quad (2)$$

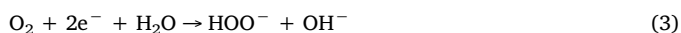
Where, *R* is the gas constant, *T* is the temperature (K), *F* is the Faraday constant, *n* is the number of electrons involved in the electrode reactions, and *i<sub>0</sub>* is the exchange current density.

The *V<sub>OC</sub>* and *I<sub>SC</sub>* output measurements were performed in 0.1 M KOH aqueous solutions using time-voltaic and time-current polarization test methods, respectively. The polarization curves were recorded with the on/off simulated solar illumination frequency of 30 s.

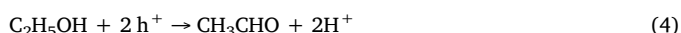
#### 2.4. Solar-driven ORR for H<sub>2</sub>O<sub>2</sub> production

The solar-driven ORR catalytic generation of H<sub>2</sub>O<sub>2</sub> on Ag NP/SG/Cu nanosandwich electrodes and reference samples of SG/Cu and Ag NP/Cu were performed with a two-electrode system containing a Pt gauze as counter electrode and as-prepared samples as working electrode in a quartz breaker chamber. The electrolyte was 0.1 M KOH and ethanol/water mixture (1/24 v/v) solution. The experiments were performed under O<sub>2</sub>-equilibrated conditions. The reaction times were controlled at 10, 20, 40, 60, 90, 120, 180, 260, 300, 360, and 420 min under simulated solar illumination.

Under simulated solar irradiation, the hot-electrons to catalyze the ORR reaction in 2-electron pathway to generate HOO<sup>-</sup> radical ions on the surface of Ag NP (Eq. (3)).



The positive hot-holes (h<sup>+</sup>) transfer and accumulate on the counter electrode. In order to ensure the ionization equilibrium in the electrolyte, the system requires ethanol as electron donors to neutralize the holes, transfer from Cu by built-in electric field at the counter electrode (Eq. (4)).



The solar-to-chemical conversion (SCC) efficiency was calculated with (Eq. (5)) [38].

$$SCC \text{ efficiency}(\%) = \frac{\Delta G \cdot V}{W_{input} \cdot t} \quad (5)$$

Where,  $\Delta G$  is the free energy for H<sub>2</sub>O<sub>2</sub> generation (117 kJ mol<sup>-1</sup>), *V* is

the volume of H<sub>2</sub>O<sub>2</sub> (mol), *W<sub>input</sub>* is the total input power (0.134 W) under simulated solar irradiation, *t* is the reaction time (s).

#### 2.5. Detection of H<sub>2</sub>O<sub>2</sub> concentration

The concentration of H<sub>2</sub>O<sub>2</sub> is the most effective means to evaluate the efficiency of the proposed photocatalytic system. Here, the peroxidase catalysed oxidation of *n*, *n*-diethyl-*p*-phenylenediamine (DPD) method has been used to estimate the concentration of H<sub>2</sub>O<sub>2</sub> [39]. 27.0 ml of sample was collected during the irradiation and piped into a 50.0 ml breaker, and 3.0 ml of the buffer solution was added with stirring to achieve pH 6.0 in the final solution. Then 50.0 μl DPD reagent solution (dissolved by 0.1 N H<sub>2</sub>SO<sub>4</sub>) and 50.0 μl of the POD reagent (dissolved by deionized water) were added with stirring was continued during the procedure. To avoid exceeding the detection limit of DPD, the sample aliquots were added in different times of dilution. The final solution was transferred into a photometric quartz cell of 1.0 cm path length after slowly stirring for 90 s. The absorption spectrum was taken from 400 to 650 nm, and the absorbance was measured at 551 nm. The calculation of H<sub>2</sub>O<sub>2</sub> concentration can be achieved by following relationship:

$$[H_2O_2]_{\text{sample}} = \frac{A_i^{551\text{nm}} \cdot V_{\text{final}}}{\epsilon \cdot l \cdot V_{\text{sample}}} \quad (6)$$

Where,

*A<sub>i</sub><sup>551nm</sup>* = the value of absorbance peak at 551 nm after correcting for blank in cell of path length *l*;

$\epsilon$  = 2100 M<sup>-1</sup> cm<sup>-1</sup> (accuracy ~ ± 2% for 95% confidence limit);

*l* = path length of photometric quartz cell;

*V<sub>final</sub>* = final volume after addition of all reagents and buffer;

*V<sub>sample</sub>* = volume of original panangin.

Because the sample aliquots were diluted in different times to avoid the detection limit of DPD, the calibration curves of the concentration of H<sub>2</sub>O<sub>2</sub> in different samples were also obtained relying on the different of samples concentration.

#### 2.6. Plasmonic near-field distribution calculations

The numerical calculations were performed using FDTD solutions (Lumerical solutions) to better understand the nature of the strong near-field enhancement. The theoretical model closely matched the actual experimental samples, i.e., a 40 nm Ag NP loaded on a 300 nm thick Cu foil directly or separated by single layer graphene and reference sample (SG/Cu). The distance between neighboring Ag NPs was about 8 nm (Fig. 4d). A perfectly matched layer was used as radiation boundary condition. The plane wave was used as source. The calculation region was 150 × 150 × 200 nm<sup>3</sup> with a conformal mesh region self-adapted to the structure.

### 3. Results and discussion

The Ag NP/SG/Cu nanosandwich electrode was fabricated according to the procedure described in Fig. 1a. The details can be found in the Experimental Section. Briefly, a single-layer graphene was prepared on the surface of Cu foil by the chemical vapor deposition method and a layer of Ag nanoparticles (Ag NPs) was deposited on the surface of graphene layer in the desktop DC ion-sputtering system. The sputtering method has been well-designed for synthesizing metal nanoparticles, which reduces the complexity of chemical synthesis processes and facilitate control over size, shape, and aggregation of the nanoparticles. Nearly monodisperse nanoparticles were synthesized by gas



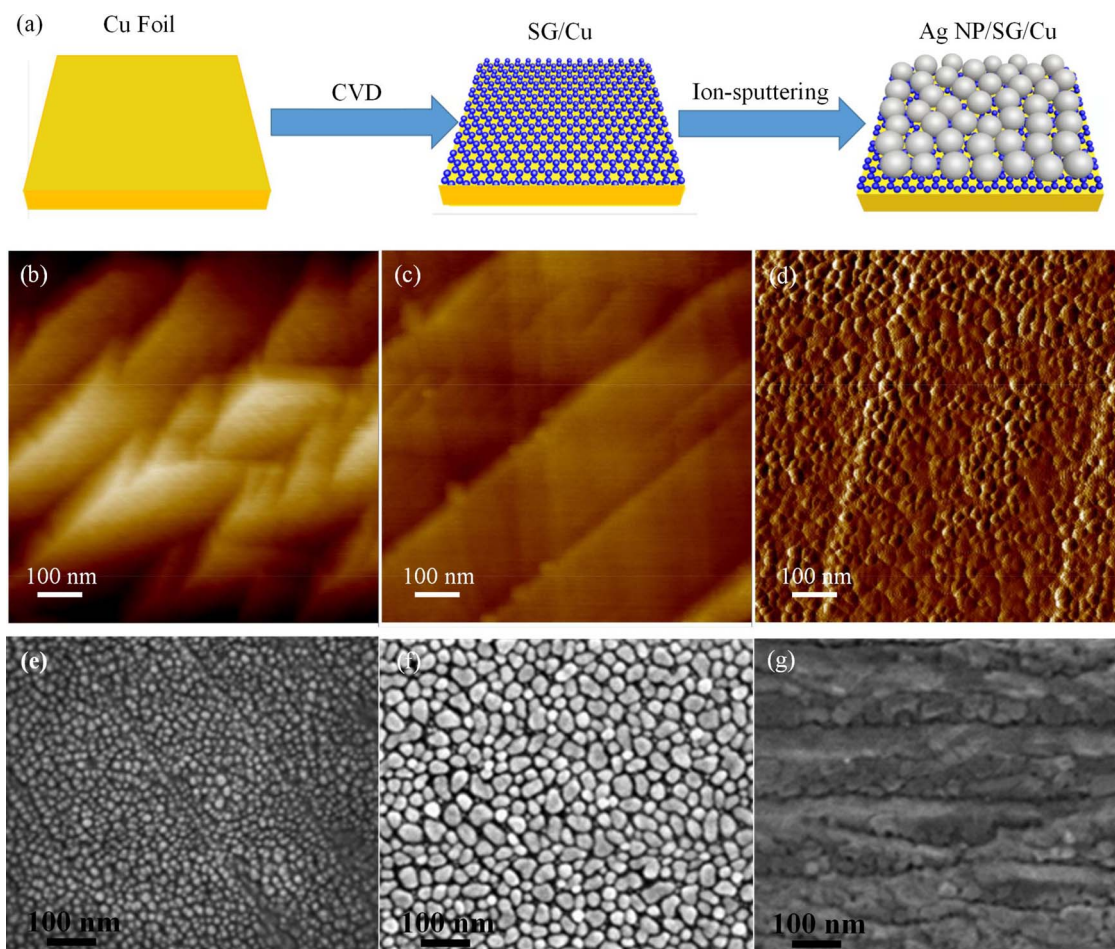


**Fig. 1.** (a) Schematic of the fabrication process for the Ag NP/SG/Cu nanosandwich electrode. The Ag nanoparticles (Ag NP) was deposited on the single-layer graphene (SG) by the ion-sputtering method, and the single-layer graphene (SG) was fabricated on the surface of Cu foil (Cu) by the chemical vapor deposition method. Tapping-mode AFM image of the typical morphologies of (b) the Cu foil, (c) the single layer graphene on the Cu foil (SG/Cu) sample, and (d) Ag nanoparticles deposited after 120 s on a graphene surface in the Ag NP/SG/Cu-120s sample. SEM images of Ag nanostructures in the Ag NP/SG/Cu nanosandwich electrodes for the deposition time of 120 s (e), 180 s (f) and 240 s (g).

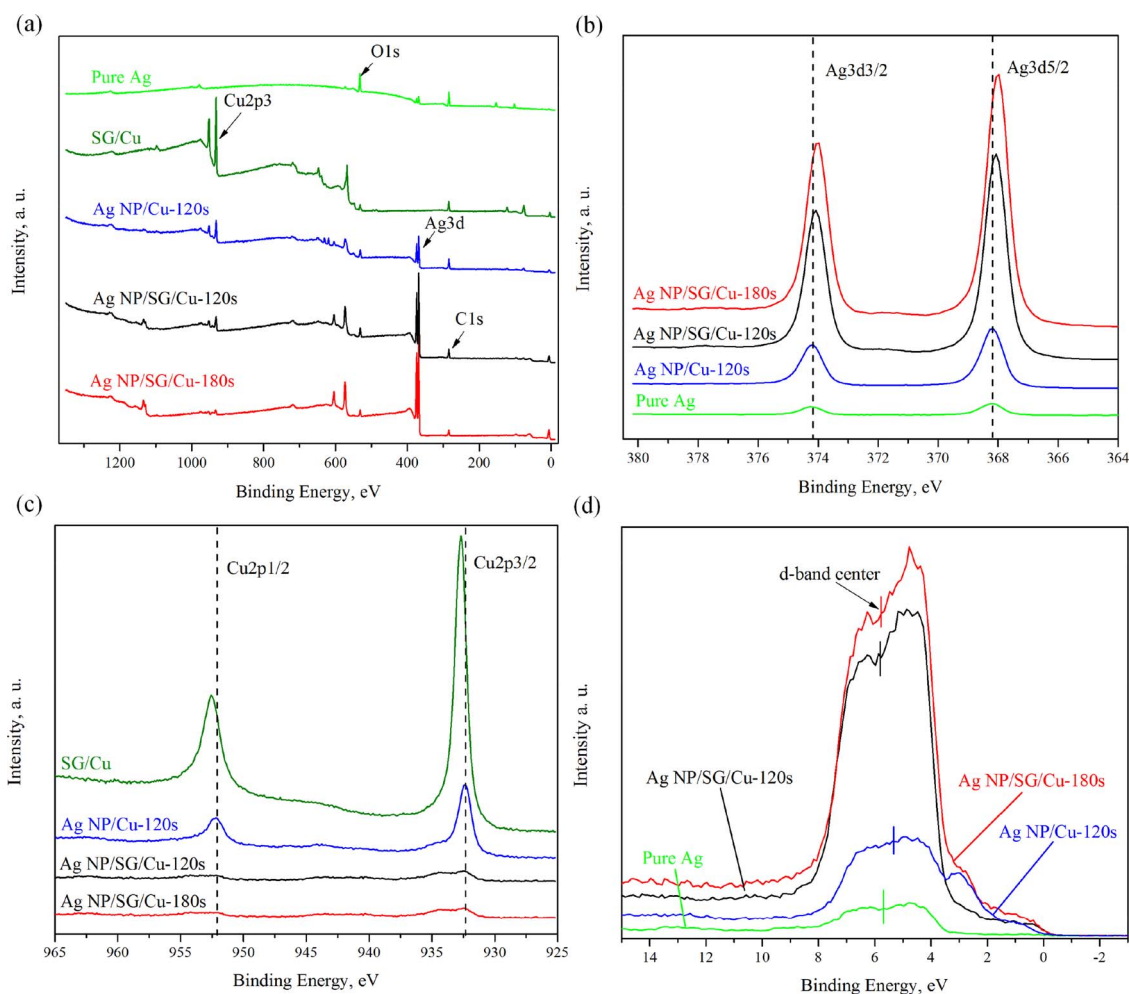
condensation of the silver vapor on a clean graphene surface at room temperature through a Volmer-Weber self-limiting growth mode [40,41], leading to a distribution of Ag nanoparticles with uniformly size and spacing on the graphene surface, where relatively uniform surface defects can serve as preferential sites for Ag cluster nucleation. The growth condition of Ag NPs during the sputtering was optimized by the different deposition time with the suitable target-substrate distance of 5 cm and the sputtering current of 5 mA. A series of the Ag NPs were prepared at the deposition time of 0, 120, 180, and 240s, and the synthesized samples were labeled as SG/Cu, Ag NP/SG/Cu-120s, Ag NP/SG/Cu-180s and Ag NP/SG/Cu-240s, respectively. As a control, the Ag NPs were prepared on the Cu foil at the deposition time of 120s, labeled as Ag NP/Cu-120s.

Fig. 1b–d shows the typical morphologies of the Cu foil, the single-layer graphene on Cu foil (SG/Cu), and the Ag NPs on the single-layer graphene with Cu contact (Ag NP/SG/Cu-120s) by atomic force microscopy (AFM), respectively. Cu foil shows a corrugated surface, as-grown graphene is uniformly layered on Cu foil with only a few stacking geometry of the bilayer in edge region, and Ag NPs are well-distributed on the graphene surface in Ag NP/SG/Cu-120s sample, which might be beneficial for the plasmonic performance. Fig. 1e,f,g display the scanning electron microscopy (SEM) images of Ag NP morphologies at the deposition time of 120, 180, and 240 s, respectively. It is shown that the Ag NPs are highly uniformly dispersed on the graphene surface in the Ag NP/SG/Cu-120s sample, and the average size of Ag NP is about 10 nm for the deposition time of 120s. In Fig. 1f, the average size of Ag NPs is about 40 nm for the deposition time of

180 s, indicating that the Ag NPs become larger when the deposition time increases. As shown in Fig. 1g, a thin film of Ag is formed on the graphene surface after a long deposition time of 240 s in the Ag NP/SG/Cu-240s sample.

A typical Raman spectra of the single-layer graphene fabricated on a Cu substrate (SG/Cu) is shown in Fig. S1a (Supporting Information). It reveals that the intensity ratio of 2D peak and G peak is 2.55, pointing out that the high uniformity and integrity of graphene [42]. Fig. S1b shows the X-ray diffraction (XRD) patterns of the Cu foil, SG/Cu, Ag NP/SG/Cu-120s, and Ag NP/SG/Cu-180s samples. It reveals that the diffraction peaks of Cu foil locate at 43.3, 50.43, and 74.13°, respectively. Two new diffraction peaks are appeared after graphene layered at 13.94 and 16.76°, respectively. Four new diffraction peaks are appeared after Ag deposited at 38.12, 44.28, and 64.43°, respectively, which could be indexed to the <111>, <100>, and <200> planes of pure silver (JCPDS No. 04-0783), demonstrating the successful deposition of Ag nanoparticle onto the single-layer graphene surface according to the fabricating procedure in Fig. 1a. Fig. S1c (Supporting Information) shows the Cu, Ag and C element mapping on the surface of the Ag NP/SG/Cu-120s sample.

Fig. 2 shows the surface deep-level electronic structures of pure Ag, Ag NPs on the graphene in the Ag NP/SG/Cu-120s sample, Ag NPs on the graphene in the Ag NP/SG/Cu-180s sample, Ag NPs on the Cu foil in the Ag NP/Cu-120s sample, and the graphene on Cu foil without Ag NPs in the SG/Cu sample by X-ray photoelectron spectroscopic (XPS). Fig. 2a shows the full XPS spectra of the pure Ag, Ag NP/SG/Cu-120s, Ag NP/SG/Cu-180s, Ag NP/Cu-120s and SG/Cu samples. It reveals that



**Fig. 2.** XPS full spectra of (a) the pure Ag, the SG/Cu, the Ag NP/SG/Cu-120s, the Ag NP/SG/Cu-180s, and the Ag nanoparticles with the deposition time of 120 s on the Cu foil (Ag NP/Cu-120s) sample. The high-resolution spectra of (b) Ag 3d, the vertical dashed lines are used to indicate the location of pure Ag 3d peaks, and (c) Cu 2p, the vertical dashed lines are used to indicate the location of pure Cu 2p peaks. (d) Valence band spectrum of the pure Ag, the Ag NP/SG/Cu-120s, the Ag NP/Cu-120s, and the Ag NP/SG/Cu-180s, samples.

the binding energies of oxygen and carbon are 530.86 and 285.05 eV, respectively, both lower than their zero-valent values, indicating that  $O_2$  and C are chemisorbed on the surface. Fig. 2b shows the high-resolution spectra of Ag 3d in the pure Ag, Ag NP/SG/Cu-120s, Ag NP/SG/Cu-180s and Ag NPs on the Cu foil in the Ag NP/Cu-120s samples, the vertical dashed lines are used to indicate the location of pure Ag 3d peaks. It reveals that the Ag 3d peaks for the Ag NPs supported on the graphene (Ag NP/SG/Cu-120s and Ag NP/SG/Cu-180s) shift slightly to the lower binding energy compared with the pure Ag, but the Ag 3d peaks for the Ag NPs supported on the Cu foil (Ag NP/Cu-120s) remains unchanged, indicating that Ag NPs and the single-layer graphene are in good contact, a possible charge transfer from the graphene to Ag NPs. Fig. 2c shows the high-resolution spectra of Cu 2p of the Cu foil with the graphene in the SG/Cu sample, Cu foil with deposited Ag nanoparticles in the Ag NP/Cu-120s, Ag NP/SG/Cu-120s, and Ag NP/SG/Cu-180s. From Fig. 2c, the Cu foil with the graphene (SG/Cu) shows that two distinct peaks are located at 952.5 and 932.7 eV, which assigns to the density of states of  $Cu2p_{1/2}$  and  $Cu2p_{3/2}$ , respectively. The Cu 2p peaks in the Ag NP/Cu-120s, Ag NP/SG/Cu-120s, and Ag NP/SG/Cu-180s samples are weaker than that of the SG/Cu sample because of surface coverage of Ag NP. Compared with the pure Cu, the Cu 2p peaks of the Cu foil with the graphene (SG/Cu) shift remarkably to higher binding energy, indicating that Cu foils are in good contact with the single layer graphene, which can facilitate the electron transfer at the interface of SG/Cu [43,44]. Moreover, Fig. 2d shows the valence band spectrum of Ag in the pure Ag, Ag NP/SG/Cu-120s, Ag NP/SG/Cu-180s, and Ag NPs

on the Cu foil in the Ag NP/Cu-120s samples. Compared with the pure Ag, both the d-band centers of the Ag NP/SG/Cu-120s and the Ag NP/SG/Cu-180s samples are slightly away from the Fermi energy level, and the d-band center of the Ag NP/Cu-120s sample is closer to the Fermi energy level. Therefore, it is clear that electronic structures of Ag NPs in the Ag NP/SG/Cu nanosandwich electrodes are modified when Ag NPs are attached to the graphene layer and Cu bottom layer, and there is a strong coupling between Ag NP, graphene layer and Cu layer in the nanosandwich of Ag-graphene-Cu catalysts.

Electron density of the Ag NPs can be further enriched via photo-excited electron-holes from plasmonic nanosandwich of Ag-graphene-Cu. Fig. 3a shows the open-circuit voltage ( $V_{OC}$ ) and short-circuit current ( $I_{SC}$ ) between on/off states for Ag NP/SG/Cu nanosandwich electrode with respect to the Pt counter electrode as switching on/off simulates solar irradiation. It shows that the polarity of the measured voltage is opposite to the current, this photoelectrical response is totally different with the conventional semiconductor-based systems, where the photoexcited  $I_{SC}$  has a zero-phase angle related to the induced voltage [45]. To separate the photoelectric response contributions from different subgroups, the  $V_{OC}$  and  $I_{SC}$  performances of the graphene (SG/Cu) and the Ag NPs (Ag NP/Cu-120s) were measured, respectively, as shown in Fig. 3a. From Fig. 3a, the  $V_{OC}$  and  $I_{SC}$  values of the sample without Ag NPs (SG/Cu) or graphene (Ag NP/Cu-120s) are much smaller than the values of Ag NP/SG/Cu-120s sample. It indicating that efficient electron-hole separation could be achieved through ultrafast charge transfer between Ag-graphene-Cu layers despite of their weak

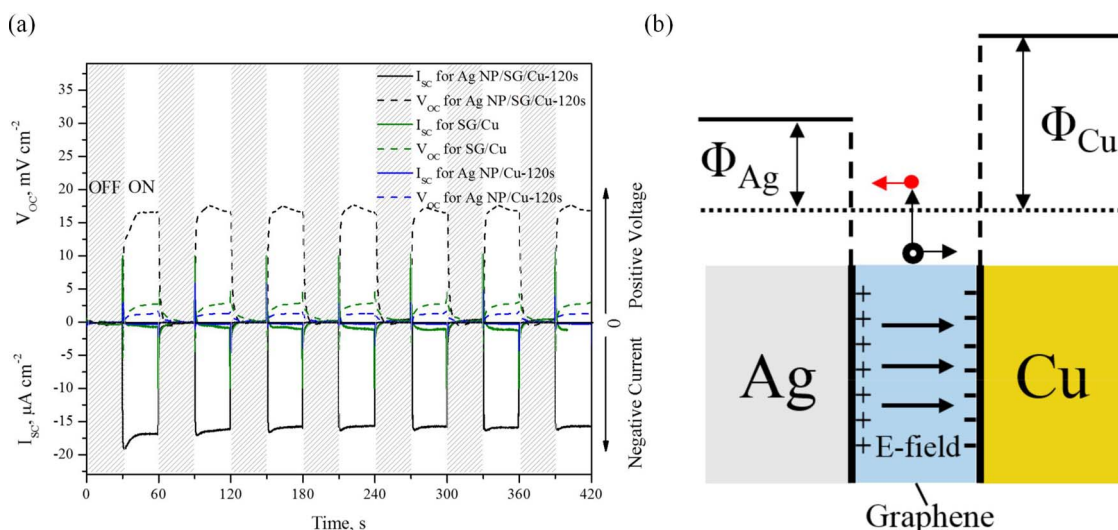


Fig. 3. (a) Photogenerated short-circuit current ( $I_{sc}$ ) and open-circuit voltage ( $V_{oc}$ ) outputs of Ag NP/SG/Cu-120s and reference samples (SG/Cu and Ag NP/Cu-120s) under on/off light modulation of a simulated solar without a bias. (b) Schematic band diagram of the Ag NP/SG/Cu nanosandwich electrode.

van der Waals interaction, which has been experimentally observed in vertically stacked  $MoS_2/WS_2$  two-dimensional heterostructure bilayers with weak van der Waals [46–48]. The electron-hole separation scheme in the Ag NP/SG/Cu nanosandwich electrode is illustrated in Fig. 3a, by absorbing visible or ultraviolet light, Ag NP generates excitons which soon separate to energetic hot electrons and holes. Specifically, the hot electrons on the Ag NP mainly localized on inner graphene sites, while holes transfer to the outer graphene layer, according to different material properties. How the electron-hole pair can overcome the interfacial Coulombic potential is the critical role of electronic delocalization, which leads to efficient charge separation with high internal quantum efficiency. Such electronic delocalization is initially formed by the built-in electric field action in the plasmonic Ag-graphene-Cu nanosandwich. In fact, when graphene is in contact with the metal, there will be electron transfer at the interface, and an interfacial dipole layer is theoretically predicted to be formed between metal and graphene [49]. Due to the existence of the interfacial dipole layer, a *p*-type or *n*-type doping of pristine graphene can be produced by the contact of metal [50]. The theoretical calculations and experiments suggest that the magnitude of the doping is dependent on the difference between the work functions of graphene and metal [51]. For the Ag NP/SG/Cu nanosandwich electrode, Ag has a much smaller work function than Cu, and therefore, a *p*-type doping in graphene via electron transfer from graphene to Ag metal accompanied with a comparatively weaker *p*-type doping in graphene via electron transfer from graphene to Cu metal, which results in a potential gradient between Ag and Cu. As shown in Fig. 3b, the potential profile in the Ag NP/SG/Cu nanosandwich electrode leads to the built-in electric field, and the electron-hole pairs are separated by the built-in electric field within the graphene, resulting in a net current from Ag to Cu through graphene. To separate the contributions from Pt gauze in the photoelectric response measurement setup, the graphite plate was used to replace Pt gauze as the counter electrode, and the values of both  $V_{oc}$  and  $I_{sc}$  show no obvious decline as shown in Fig. S2 (Supporting Information).

In order to understand and ensure that the light absorption of Ag NP/SG/Cu nanosandwich electrode is mainly contributed by the SPR of Ag NPs, we also measured the diffuse reflectance UV–vis absorption spectra of Cu foil, the Ag NP/SG/Cu-120s, the Ag NP/SG/Cu-180s, Ag NPs on the Cu foil without graphene (Ag NP/Cu-120s) and the graphene on Cu foil (SG/Cu) in Fig. 4a. The Cu foil shows a weak absorption ranging from 350 to 550 nm wavelength, and a broad absorbance peak around 500 nm wavelength is appeared after graphene deposition on Cu foil. An absorption peak at 400–430 nm wavelength appears in the

diffuse reflectance UV–vis absorption spectra of the Ag NP/SG/Cu-120s, the Ag NP/SG/Cu-180s, and the Ag NP/Cu-120s samples, which can be attributed to the SPR absorption of Ag NPs after the deposition of Ag NPs on SG/Cu and Cu foil. The absorption around 500 nm is obviously from the graphene. Fig. S3a (Supporting Information) shows the SPR absorption peak of the Ag NPs aqueous solution, the Ag NP/SG/Cu-120s, the Ag NP/SG/Cu-180s and the Ag NP/SG/Cu-240s samples, the Ag NP/SG/Cu-180s sample exhibits a higher absorption peak than that of the Ag NP/Cu-120s, the Ag NP/SG/Cu-120s and the Ag NP/SG/Cu-240s samples in 400–430 nm wavelength, indicating that the Ag NP density indeed effects the light harvesting. To further confirm the SPR of Ag NPs effect on the photocurrent generation of Ag NP/SG/Cu nanosandwich electrode, two monochromatic LED light sources were used to investigate the effect of the light wavelength on the photocurrent generation. Fig. 4b shows that the photocurrent density of  $12.4 \mu A cm^{-2}$  at an irradiation wavelength of 418 nm is 6 times higher than that at 580 nm in the Ag NP/SG/Cu-120s sample, indicating that the SPR was excited in the Ag NPs. Fig. 4c and Fig. S3c (Supporting Information) present the effect of the light wavelength (418 nm, 580 nm) on the photocurrent generation parallel tests in the Ag NP/SG/Cu-180s and the Ag NP/SG/Cu-240s samples, respectively, the similar trends can be achieved when compared with the photocurrent of the Ag NP/SG/Cu-120s sample. These results indicate that the SPR of Ag NPs in 400–430 nm wavelength has an important contribution to the photocurrent generation of Ag NP/SG/Cu nanosandwich electrodes. To better understand the fundamentals of the strong near-field enhancement in the Ag NP/SG/Cu nanosandwich electrode, the plasmonic near-field distribution were calculated by FDTD method in the Ag NP/SG/Cu nanosandwich electrode at the resonant wavelength of 418 nm. Both Fig. 4d and Fig. S3d (Supporting Information) show the plasmonic coupling occurs between the Ag NPs and the gap of the Ag NPs and Cu substrate when they are separated by graphene sub-nanospace at the resonant wavelengths. The multiple plasmonic couplings are also observed clearly between the closely distributed Ag NPs, as shown in Fig. 4d. When many Ag NPs bring together with very small gap of 8 nm sitting on graphene/Cu substrate, the enhanced field strength with local EF value of  $1.01 \times 10^{29}$  is obtained at the small gap. The hot spot has also appeared at the sub-nanospace between the Ag NPs and Cu substrate as well as between the closely distributed Ag NPs. As the local field strength (EF) is  $1.63 \times 10^{29}$  in Ag NP/SG/Cu with cross-sectional (see Fig. S3d, Supporting Information). These results indicate that the plasmonic coupling plays a very important role in the Ag NP/SG/Cu and considerably strengthens the near-field on the graphene spacer



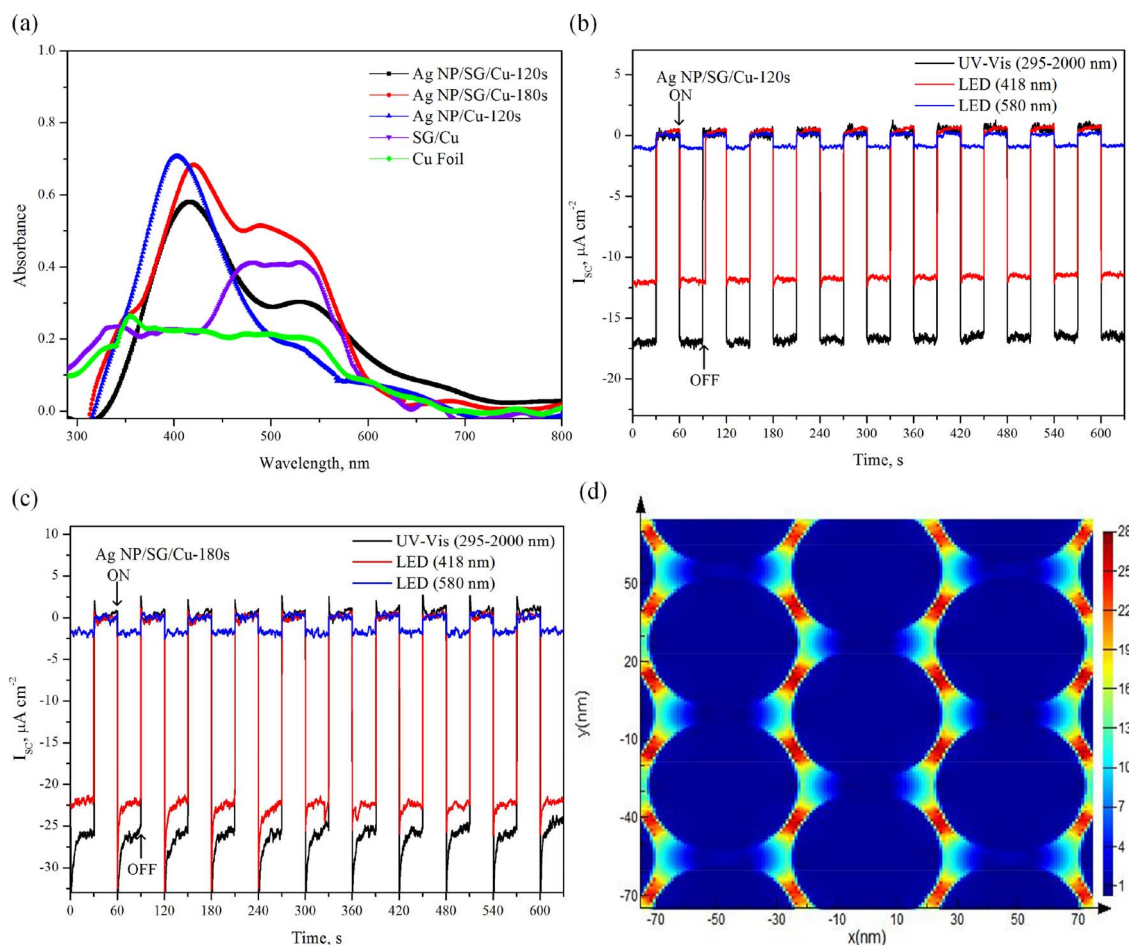


**Fig. 4.** (a) Diffuse reflectance UV–vis absorption spectra of the Cu foil, SG/Cu, Ag NP/Cu-120s, Ag NP/SG/Cu-120s, and Ag NP/SG/Cu-180 s samples.  $I_{sc}$  outputs of (b) the Ag NP/SG/Cu-120s sample, and (c) the Ag NP/SG/Cu-180s sample with UV–vis (simulated solar), LED (418 nm), and LED (580 nm) irradiation, respectively. (d) Top-viewed plasmonic near-field distribution of the Ag NP/SG/Cu nanosandwich electrode at excitation wavelength of 418 nm. The electrical field was investigated using FDTD method.

layer for the generation of electron-hole pair. As a result of this plasmonic coupling in Ag NP/SG/Cu, we observe a significant improvement in the photogenerated voltage and current in Ag NP/SG/Cu nanosandwich electrode.

Like the photocatalytic generation of  $H_2O_2$  from the binary plasmonic metal and semiconductor hybrid catalyst systems, the efficient separation of photoexcited electron-hole pairs in Ag NP/SG/Cu is proven to be used for a two-electron oxygen reduction reactions without applying an external bias. Fig. 5a shows the time-dependent changes in the  $H_2O_2$  concentrations for the Ag NP/SG/Cu-120s, Ag NP/

SG/Cu-180s, Ag NP/SG/Cu-240s, Ag NPs on the Cu foil without graphene (Ag NP/Cu-120s), and graphene on Cu foil without Ag NPs (SG/Cu). As shown in Fig. 5, the yield of hydrogen peroxide is about 200  $\mu M$  in first 90 min, after that, the concentration of  $H_2O_2$  still increases when the reaction continues, however, the rate is smaller than that of the starting moments, it proves that the formation and decomposition rates follow the zero-order and first-order kinetics in the photocatalytic generation of  $H_2O_2$ , respectively. Under the constant concentration of dissolved oxygen and the stable light irradiation, the rate of photocatalytic formation of  $H_2O_2$  on Ag NP/SG/Cu is regarded as zero-order

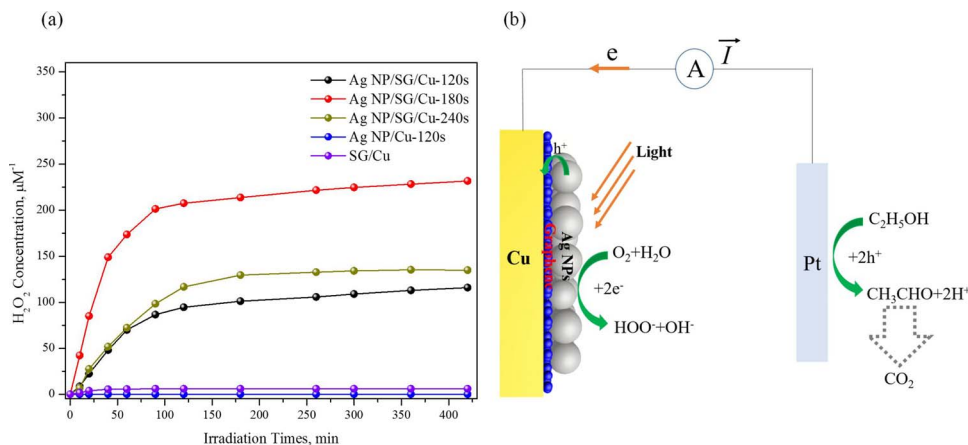


**Fig. 5.** (a) Photocatalytic generation of hydrogen peroxide ( $H_2O_2$ ) under  $O_2$ -equilibrated conditions with the samples of the Ag NP/SG/Cu nanosandwich electrodes (Ag NP/SG/Cu-120s, Ag NP/SG/Cu-180s, and Ag NP/SG/Cu-240s) and the reference samples (SG/Cu and Ag NP/Cu-120s). (b) Scheme of  $H_2O_2$  generation of the Ag NP/SG/Cu nanosandwich electrode after irradiated by the simulated solar. The alcohol was used as the electron donor.

**Table 1**Performance parameters for H<sub>2</sub>O<sub>2</sub> photocatalytic generation, photocurrent, photovoltage, and solar-to-chemical conversion (SCC) efficiency.

Material	Photocurrent ( $\mu\text{A cm}^{-2}$ )	Photovoltage ( $\text{mV cm}^{-2}$ )	Yield of H <sub>2</sub> O <sub>2</sub> ( $\mu\text{M}$ , 2 h)	SCC efficiency (%)	References
Ag NP/SG/Cu	15.8	17.5	187.68	0.97	This work
g-C <sub>3</sub> N <sub>4</sub> /PDI	0.32	–	210.86	1.09	[54]
rGO/TiO <sub>2</sub> /CoPi	–	–	73.8	0.38	[14]
Au <sub>0.2</sub> /BiVO <sub>4</sub>	1.5	–	40	0.21	[52]
rGO/TiO <sub>2</sub> /WO <sub>3</sub>	–	–	16.7	0.09	[57]
g-C <sub>3</sub> N <sub>4</sub> /PDI/rGO <sub>0.05</sub>	0.52	–	39.6	0.2	[53]
CuO	–	–	5	0.013	[58]
BiVO <sub>4</sub> + [Ru <sup>II</sup> ((MeO) <sub>2</sub> bpy) <sub>3</sub> ] <sup>2+</sup>	300	–	125.6	0.65	[59]

kinetic (Eq. (7)):

$$\frac{d[\text{H}_2\text{O}_2]_f}{dt} = k_f \quad (7)$$

Where, the  $k_f$  is the H<sub>2</sub>O<sub>2</sub> formation rate constant,  $[\text{H}_2\text{O}_2]_f$  is the theoretical concentration of H<sub>2</sub>O<sub>2</sub>.

However, the decomposition rates of H<sub>2</sub>O<sub>2</sub> in the solutions need be considered, which can be assuming as pseudo first-order kinetic (Eq. (8)):

$$\frac{d[\text{H}_2\text{O}_2]_f}{dt} = k_d[\text{H}_2\text{O}_2]_d \quad (8)$$

Where, the  $k_d$  is the H<sub>2</sub>O<sub>2</sub> decomposition rate constant,  $[\text{H}_2\text{O}_2]_d$  is the concentration of H<sub>2</sub>O<sub>2</sub> in the solution.

Subsequently, the function of H<sub>2</sub>O<sub>2</sub> concentration variation with reaction time is given by Eq. (9):

$$[\text{H}_2\text{O}_2] = \frac{k_f}{k_d} \{1 - \exp(-k_d t)\} \quad (9)$$

The amount of produced H<sub>2</sub>O<sub>2</sub> in Ag NP/SG/Cu-180 s sample reached ca 229.33  $\mu\text{M}$  after the simulated solar irradiation for 420 min. Table 1 compares the H<sub>2</sub>O<sub>2</sub> generation performance with the state-of-the-art literature data in terms of the photocurrent, photovoltage, and solar-to-chemical conversion (SCC) efficiency. The yield from Ag NP/SG/Cu-180 s is much larger than that of most previously reported photocatalysts, including the Au<sub>0.2</sub>/BiVO<sub>4</sub> [52], the g-C<sub>3</sub>N<sub>4</sub>/PDI/rGO [53], and is comparable to the g-C<sub>3</sub>N<sub>4</sub>/PDI nanohybrid photocatalyst [54]. The similar enhancement on photocatalytic activity was observed in other Ag NP/SG/Cu nanosandwich electrodes. In contrast, for the electrode sample without single-layer graphene (SG) or Ag NPs shows a very low yield (< 0.2  $\mu\text{M}$ ). It is therefore determined that the efficient electron-hole separation could be achieved through Ag-graphene layers due to the built-in electric field in the Ag NP/SG/Cu nanosandwich electrode. The H<sub>2</sub>O<sub>2</sub> generation scheme in the Ag NP/SG/Cu nanosandwich electrode is illustrated in Fig. 5b. After irradiated by the simulated solar, Ag NPs generates excitons, which soon separates energetic electrons and holes. Specifically, hot-electrons on the Ag NPs surface initialize the ORR reaction by 2-electron pathway and produce the H<sub>2</sub>O<sub>2</sub>, where H<sub>2</sub>O<sub>2</sub> exists as HOO<sup>−</sup> in alkaline solution [55]. The holes from SPR excitement are energetic enough to oxidize ethanol. Ethanol acts as the electron donor and is oxidized on the Pt surface for neutralization of positive hot holes. To separate the effect of Pt gauze on the catalytic generation of H<sub>2</sub>O<sub>2</sub>, the graphite plate was used to replace Pt gauze as counter electrode. The same yield of H<sub>2</sub>O<sub>2</sub> is obtained after the illumination for 420 min with the sample of Ag NP/SG/Cu-180 s as working electrode (see Fig. S4a, Supporting Information). It is noteworthy that, compared with the time of H<sub>2</sub>O<sub>2</sub> production on the Ag NP/SG/Cu-120s, Ag NP/SG/Cu-180s, and Ag NP/SG/Cu-240 s samples, respectively, the photocatalytic H<sub>2</sub>O<sub>2</sub> formation rate of Ag NP/SG/Cu-180 s is higher than the other two though it has a large particle size (40 nm) than the Ag NP/SG/Cu-120 s (10 nm). The low H<sub>2</sub>O<sub>2</sub> formation rate in the Ag NP/SG/Cu-240 s is obvious due to the low surface specific area related to the typical morphology of Ag thin film. The photocatalytic stability of Ag NP/SG/Cu nanosandwich electrode is further

evaluated by a cycling experiment. Fig. S4b shows the yield of H<sub>2</sub>O<sub>2</sub> as function of cycle number on Ag NP/SG/Cu-180 s sample, and the catalyst was repeatedly used for 1, 2, 3, 4, 6, 8, and 10 cycles with a time step of 420 min. The yield of H<sub>2</sub>O<sub>2</sub> shows a loss of 22.51% for Ag NP/SG/Cu-180 s after 10 cycles of photocatalyzed H<sub>2</sub>O<sub>2</sub> generation reaction. The structure stability is evaluated by comparing the XRD and FE-SEM results for the Ag NP/SG/Cu-180 s before and after 10 cycles in Fig. S5, it is clear that no obvious changes in XRD peak location and nanoparticle morphology were observed after 10 cycle experiment, indicating that the Ag NP/SG/Cu-180 s possess a good structural stability.

To further understand the catalytic mechanism of H<sub>2</sub>O<sub>2</sub> generation on the plasmonic nanosandwich of Ag-graphene-Cu, the electrochemical properties of Ag NP/SG/Cu and reference samples were studied by RDE measurements. Fig. 6a shows the ORR curves of the Ag NP/SG/Cu-120s, Ag NP/SG/Cu-180s, Ag NP/SG/Cu-240s, Ag NPs on the Cu foil without graphene (Ag NP/Cu-120s) and graphene on Cu foil without Ag NPs (SG/Cu). In dark, the Ag NP/SG/Cu nanosandwich electrodes exhibit both higher kinetic current density and more positive half-wave potential than the reference samples (SG/Cu and Ag NP/Cu-120s). Under the simulated solar irradiation, the Ag NP/SG/Cu-120 s and Ag NP/SG/Cu-240 s samples exhibit an obvious positive shift in half-wave potential but no such shift was observed in Ag NP/SG/Cu-180 s at the rotation rate of 1600 rpm. To investigate the effect of light irradiation on ORR kinetics of the Ag NP/SG/Cu and reference samples, a set of ORR curve were measured at different rotation rates (Fig. S6a–e, Supporting Information). Compared to the Ag NP/SG/Cu-180s, the sample of Ag NP/SG/Cu-120 s exhibits a higher kinetic current density and more positive half-wave potential whereas the Ag NP/SG/Cu-240 s sample exhibits a lower kinetic current density and more negative half-wave potential with respect to the others. In order to further confirm the light induced phenomena in ORR activity, a control measurement for all samples were conducted in the identical condition while the amperometric i-t mode was carried out to obtain the light induced effects upon limiting current at 0.25 V vs RHE. As illustrated in Fig. 6b, the simulated solar irradiation can generate remarkable effect upon the limiting current density of all samples with Ag NPs decorated except for SG/Cu sample, indicating that ORR activity is tuned by SPR of Ag NPs under light irradiation, the Ag NP/SG/Cu-180 s sample exhibits a higher limiting current density than all other electrode with  $\Delta j = 0.8 \text{ mA cm}^{-2}$ . To estimate the pathway selectivity of the ORR reactions, the number of transferred electrons was evaluated for all samples. Fig. 6c shows the Koutecky-Levich plots of the ORR curves at a constant electrode potential at 0.25 V vs RHE. From Koutecky-Levich slope, the number of electrons transferred ( $n$ ) in the ORR process was calculated. In the dark, the  $n$  value of 2.37 for Ag NP/SG/Cu-180 s and 2.32 for Ag NP/SG/Cu-240 s samples indicate that both two nanosandwich electrodes can catalyze the ORR reaction by 2-electron transfer pathway.  $n$  value of 3.49 for Ag NP/SG/Cu-120 s sample indicates that the ORR reaction is catalysed by two and four-electron mixed pathway. Under the light irradiation, the  $n$  value for Ag NP/SG/Cu-120 s sample rises to 3.69,  $n = 2.39$  for Ag NP/SG/Cu-180 s and  $n = 2.33$  for Ag NP/SG/Cu-240s, indicating that the effect of light



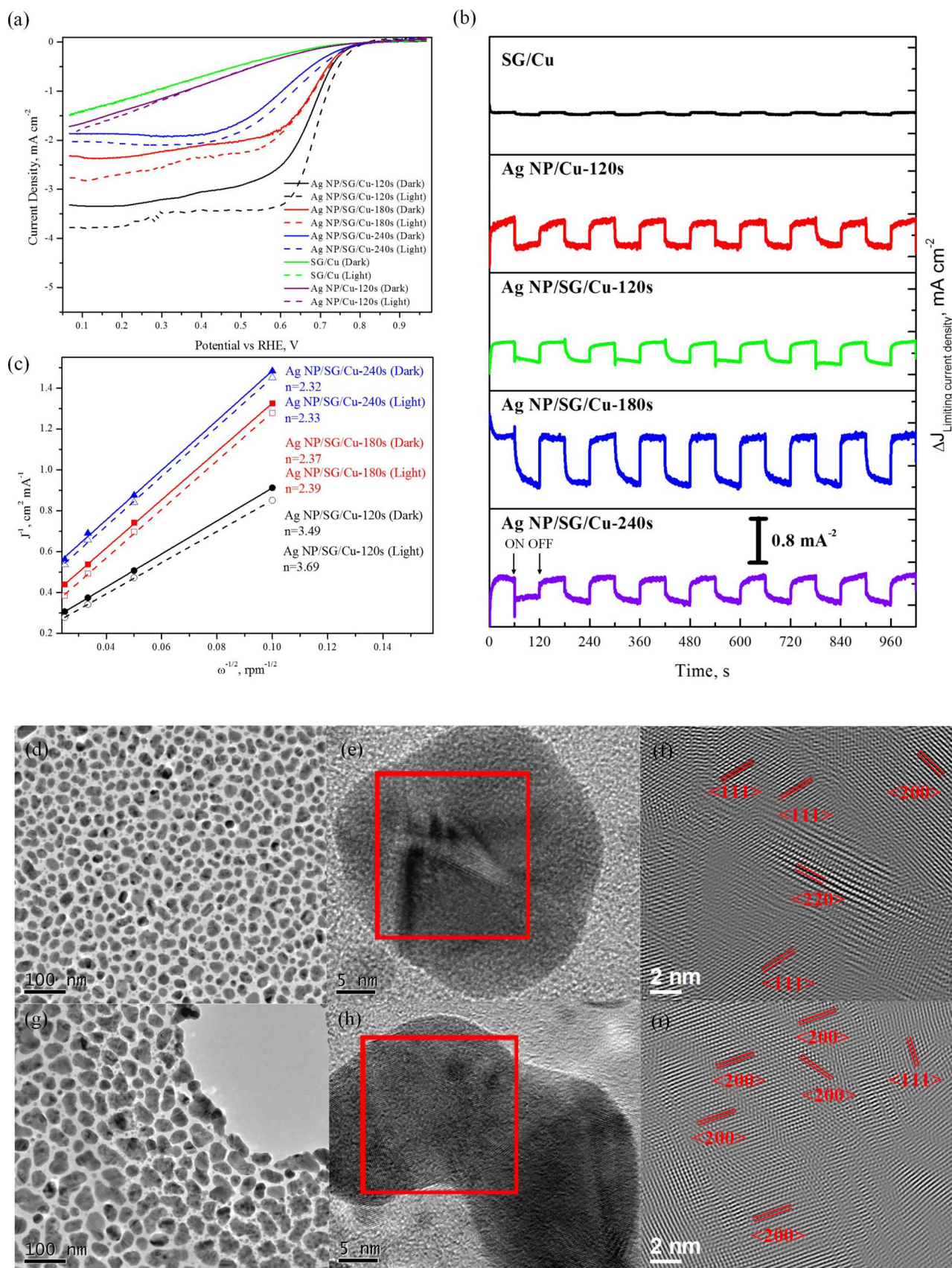


**Fig. 6.** (a) Effect of the light irradiation on oxygen reduction reaction (ORR) activity. (b) Effect of the light irradiation on the limiting current density ( $\Delta J$ ) at  $0.25 V_{\text{RHE}}$  for the Ag NP/SG/Cu nanosandwich electrodes (Ag NP/SG/Cu-120s, Ag NP/SG/Cu-180s, and Ag NP/SG/Cu-240s) and the reference samples (SG/Cu and Ag NP/Cu-120s). (c) Electron transfer number for the Ag NP/SG/Cu nanosandwich electrodes (Ag NP/SG/Cu-120s, Ag NP/SG/Cu-180s, and Ag NP/SG/Cu-240s). TEM, HRTEM and corresponding inverse fast Fourier transform images of Ag NPs in Ag NP/SG/Cu-120s (d-f) and Ag NP/SG/Cu-180s (e-i) samples.

irradiation on the pathway selectivity is negligible as compared to the limiting current density. It is clear that the Ag NP/SG/Cu-180 s sample can catalyze the ORR reaction by 2-electron transfer pathway to produce the  $\text{H}_2\text{O}_2$  under the light irradiation.

To understand the different ORR performance of the plasmonic Ag NP/SG/Cu nanosandwich electrodes, the surface structure of Ag NPs with the deposition time of 120 s and 180 s were studied by the TEM, HRTEM and the corresponding inverse fast Fourier transform (IFFT) images, as shown in Fig. 6d–i, the TEM images of Ag NPs in Fig. 6d and g with the different deposition time of 120 s and 180 s reveal that the average size of Ag NPs increases with the prolonged deposition time. Fig. 6e, show the HRTEM and IFFT image of Ag NPs with deposition time of 120s, the lattice fringes of 0.235 nm in the Ag NPs agree with those of standard Ag  $\langle 111 \rangle$  spacing of pure Ag (JCPDS 04-0783, 0.2359 nm), as seen in Fig. 6i, when the deposition time of Ag NPs is prolonged to 180 s, the  $\langle 111 \rangle$  facet of Ag NPs is disappeared, whereas, the presence of  $\langle 200 \rangle$  facet of Ag NPs can be observed, the weaker  $\text{O}_2$  absorption on Ag  $\langle 200 \rangle$  facet is the origin of the two-electron ORR activity in the Ag NP/SG/Cu-180 s sample, which promotes the reaction path way involving the formation of  $\text{H}_2\text{O}_2$ . Our previous work by Qaseem et al. [56] reviewed the structural sensitivity of Ag towards the ORR, the ORR activities of different Ag facet is related to the adsorption strengths of OH and  $\text{O}_2$  on Ag facets. The stronger affinities of OH and  $\text{O}_2$  absorption on Ag  $\langle 110 \rangle$  facet leads to a higher ORR activity compared with Ag  $\langle 111 \rangle$  and Ag  $\langle 100 \rangle$  facets. Moreover, the weaker affinities of OH and  $\text{O}_2$  on the absorption of Ag  $\langle 100 \rangle$  facet lead to a lower coverage of  $\text{OH}^-$  and  $\text{O}_2$ . These results reveal that the ORR activity of Ag crystal facets increases in the order  $\langle 110 \rangle > \langle 111 \rangle > \langle 100 \rangle$ . In this work, although the Ag NPs is prepared by the similar sputtering method, the surface structures of Ag NP are changed with different deposition times, so the variation of ORR performance of the plasmonic Ag NP/SG/Cu nanosandwich electrodes is understandable. Charge transfer resistance ( $R_{\text{CT}}$ ) across the catalyst/electrolyte interface of the Ag NP/SG/Cu nanosandwich electrode has also been investigated by electrochemical impedance spectroscopy (EIS) under simulated solar irradiation. As shown in Fig. S7 (Supporting Information), the semi-circle EIS diagrams can be achieved in all of the prepared Ag NP/SG/Cu nanosandwich electrodes and reference samples (SG/Cu and Ag NP/Cu-120s). The  $R_{\text{CT}}$  values of Ag NP/SG/Cu-120s, Ag NP/SG/Cu-180s, and Ag NP/SG/Cu-240 s are 1429, 894, and 1791  $\Omega$ , respectively, which are smaller than both Ag NP/Cu-120 s (3272  $\Omega$ ) and SG/Cu (2287  $\Omega$ ) samples. This clearly suggests that the electron-hole pairs can be generated by SPR decay of Ag NPs and separated by the built-in electric field within the graphene layer in Ag NP/SG/Cu nanosandwich electrode. This can induce more hot-electrons transferring from Ag NPs into electrolyte. In addition, the  $R_{\text{CT}}$  value of the Ag NP/SG/Cu-240 s sample is larger than both Ag NP/SG/Cu-120 s and Ag NP/SG/Cu-180 s samples, which further explains the SPR of Ag NPs can be used to affect the generation of hot-electrons in photocatalytic process.

#### 4. Conclusions

In summary, we have demonstrated that Ag NP/SG/Cu nanosandwich electrode can be constructed to generate photocurrent. We also show a new transfer path for hot-electrons catalysed ORR reaction by two-electron pathway to generate  $\text{H}_2\text{O}_2$ . It is the first demonstration, to the best of our knowledge, of the solar-driven ORR for the  $\text{H}_2\text{O}_2$  generation using graphene with asymmetrical metal contact. In addition, the present nanosandwich electrode of Ag NP/SG/Cu without any semiconductor demonstrates a possibility for converting efficient solar energy to chemical energy ( $\text{H}_2\text{O}_2$ ). From ORR activity and crystal structure studies, the mechanism of photocatalytic production of  $\text{H}_2\text{O}_2$  based on Ag NP/SG/Cu nanosandwich electrode was confirmed. The built-in electric field is believed to be the driving force to separate electron-hole pairs generated by SPR effect of Ag NPs. This process enhances the yield of hot-electrons for ORR reaction. Nevertheless, Ag

NPs surface facet can also affect the pathway selectivity for hot-electrons catalysed the ORR reaction.

#### Acknowledgements

This study was supported by the National Natural Science Foundation of China (grant nos. 51271148 and 50971100), the Research Fund of State Key Laboratory of Solidification Processing in China (grant no. 150-ZH-2016), the Aeronautic Science Foundation Program of China (grant no. 2012ZF53073), the Science and Technology Innovation Fund of Western Metal Materials (grant no. XBCL-2-11) and the Doctoral Fund of Ministry of Education of China (grant no. 20136102110013).

#### References

- [1] T.A. Fauce, W. Lubitz, A.W. Rutherford, D.R. MacFarlane, G.F. Moore, P.D. Yang, D.G. Nocera, T.A. Moore, D.H. Gregory, S. Fukuzumi, K.B. Yoon, F.A. Armstrong, M.R. Wasielewski, S. Styring, *Energy Environ. Sci.* 6 (2013) 695–698.
- [2] K. Maeda, M. Higashi, D.L. Lu, R. Abe, K. Domen, *J. Am. Chem. Soc.* 132 (2010) 5858–5868.
- [3] S. Dutta, *J. Ind. Eng. Chem.* 20 (2014) 1148–1156.
- [4] S. Fukuzumi, Y. Yamada, K.D. Karlin, *Electrochim. Acta* 82 (2012) 493–511.
- [5] J.M. Campos-Martin, G. Blanco-Brieva, J.L.G. Fierro, *Angew. Chem. Int. Ed.* 45 (2006) 6962–6984.
- [6] J.K. Edwards, B. Solsona, E. Ntainjua, N.A.F. Carley, A.A. Herzing, C.J. Kiely, G.J. Hutchings, *Science* 323 (2009) 1037–1041.
- [7] K. Mori, A. Hanafusa, M. Che, H. Yamashita, *J. Phys. Chem. Lett.* 1 (2010) 1675–1678.
- [8] S. Kato, J.U. Jung, T. Suenobu, S. Fukuzumi, *Energy Environ. Sci.* 6 (2013) 3756–3764.
- [9] Y. Shiraiishi, S. Kanazawa, Y. Kofuji, H. Sakamoto, S. Ichikawa, S. Tanaka, T. Hirai, *Angew. Chem. Int. Ed.* 53 (2014) 13454–13459.
- [10] R.X. Cai, Y. Kubota, A. Fujishima, *J. Catal.* 219 (2003) 214–218.
- [11] M. Piccinini, E. Ntainjua, J.K. Edwards, A.F. Carley, J.A. Moulijn, G.J. Hutchings, *Phys. Chem. Chem. Phys.* 12 (2010) 2488–2492.
- [12] Y. Shiraiishi, S. Kanazawa, D. Tsukamoto, A. Shiro, Y. Sugano, T. Hirai, *ACS Catal.* 3 (2013) 2222–2227.
- [13] V. Maurino, C. Minero, G. Mariella, E. Pelizzetti, *Chem. Commun.* (2005) 2627–2629.
- [14] G.-H. Moon, W. Kim, A.D. Bokare, N.-E. Sung, W. Choi, *Energy Environ. Sci.* 7 (2014) 4023–4028.
- [15] D.F. Swearer, R.K. Leary, R. Newell, S. Yazdi, H. Robatjazi, Y. Zhang, D. Renard, P. Nordlander, P.A. Midgley, N.J. Halas, E. Ringe, *ACS Nano* 11 (2017) 10281–10288.
- [16] G. Jiang, X. Li, M. Lan, T. Shen, X. Lv, F. Dong, S. Zhang, *Appl. Catal. B: Environ.* 205 (2017) 532–540.
- [17] H. Wang, F. Chen, W. Li, T. Tian, *J. Power Sources* 287 (2015) 150–157.
- [18] L.W. Zhang, L.O. Herrmann, J.J. Baumberg, *Sci. Rep.-Uk* 5 (2015).
- [19] M.R. Khan, T.W. Chuan, A. Yousuf, M.N.K. Chowdhury, C.K. Cheng, *Catal. Sci. Technol.* 5 (2015) 2522–2531.
- [20] S. Linic, P. Christopher, D.B. Ingram, *Nat. Mater.* 10 (2011) 911–921.
- [21] F. Wang, N.A. Melosh, *Nano Lett.* 11 (2011) 5426–5430.
- [22] X.J. Wen, C.G. Niu, L. Zhang, D.W. Huang, G.M. Zeng, *Ceram. Int.* 43 (2017) 1922–1929.
- [23] X.J. Wen, C.G. Niu, M. Ruan, L. Zhang, G.M. Zeng, *J. Colloids Interface Sci.* 497 (2017) 368–377.
- [24] M. Teranishi, S. Naya, H. Tada, *J. Am. Chem. Soc.* 132 (2010) 7850.
- [25] K. Qian, B.C. Sweeny, A.C. Johnston-Peck, W.X. Niu, J.O. Graham, J.S. DuChene, J.J. Qiu, Y.C. Wang, M.H. Engelhard, D. Su, E.A. Stach, W.D. Wei, *J. Am. Chem. Soc.* 136 (2014) 9842–9845.
- [26] H. Kobayashi, M. Teranishi, R. Negishi, S. Naya, H. Tada, *J. Phys. Chem. Lett.* 7 (2016) 5002–5007.
- [27] L.M. Guo, K. Liang, K. Marcus, Z. Li, L. Zhou, P.D. Mani, H. Chen, C. Shen, Y.J. Dong, L. Zhai, K.R. Coffey, N. Orlovskaya, Y.H. Sohn, Y. Yang, *ACS Appl. Mater. Interface* 8 (2016) 34970–34977.
- [28] X.-J. Wen, C.-G. Niu, D.-W. Huang, L. Zhang, C. Liang, G.-M. Zeng, *J. Catal.* 355 (2017) 73–86.
- [29] C.G. Silva, R. Juarez, T. Marino, R. Molinari, H. Garcia, *J. Am. Chem. Soc.* 133 (2011) 595–602.
- [30] A. Truppi, F. Petronella, T. Placido, M. Striccoli, A. Agostiano, M. Curri, R. Comparelli, *Catalysts* 7 (2017) 100.
- [31] C. Clavero, *Nat. Photonics* 8 (2014) 95–103.
- [32] Q. Xiao, S. Sarina, A. Bo, J. Jia, H. Liu, D.P. Arnold, Y. Huang, H. Wu, H. Zhu, *ACS Catal.* 4 (2014) 1725–1734.
- [33] M.L. Brongersma, N.J. Halas, P. Nordlander, *Nat. Nanotechnol.* 10 (2015) 25–34.
- [34] S.C. Lin, C.S. Hsu, S.Y. Chiu, T.Y. Liao, H.M. Chen, *J. Am. Chem. Soc.* 139 (2017) 2224–2233.
- [35] X. Wu, F. Chen, Y. Jin, N. Zhang, R.L. Johnston, *ACS Appl. Mater. Interfaces* 7 (2015) 17782–17791.
- [36] S.G. Canagaratna, *J. Electroanal. Chem.* 108 (1980) 371–372.

- [37] C.R. Bradbury, J.J. Zhao, D.J. Fermin, *J. Phys. Chem. C* 112 (2008) 10153–10160.
- [38] Y. Sasaki, H. Nemoto, K. Saito, A. Kudo, *J. Phys. Chem. C* 113 (2009) 17536–17542.
- [39] H. Bader, V. Sturzenegger, J. Hoigne, *Water Res.* 22 (1988) 1109–1115.
- [40] G.M. Francis, L. Kuipers, J.R.A. Cleaver, R.E. Palmer, *J. Appl. Phys.* 79 (1996) 2942–2947.
- [41] L.L. Wang, X.C. Ma, Y. Qi, P. Jiang, J.F. Jia, Q.K. Xue, J. Jiao, X.H. Bao, *Ultramicroscopy* 105 (2005) 1–5.
- [42] X. Li, J. Li, X. Zhou, Y. Ma, Z. Zheng, X. Duan, Y. Qu, *Carbon* 66 (2014) 713–719.
- [43] J.F. Moulder, R.C.K. John, J. Chastain Jr. (Eds.), *Handbook of X-ray Photoelectron Spectroscopy: A Reference Book of Standard Spectra for Identification and Interpretation of XPS Data*, Physical Electronics, Eden Prairie, Minn, 1995.
- [44] B. Jiang, C. Tian, G. Song, W. Chang, G. Wang, Q. Wu, H. Fu, *J. Mater. Sci.* 48 (2012) 1980–1985.
- [45] S. Giménez, J. Bisquert, *Photoelectrochemical Solar Fuel Production: From Basic Principles to Advanced Devices*, Springer International Publishing, 2016.
- [46] X. Hong, J. Kim, S.F. Shi, Y. Zhang, C. Jin, Y. Sun, S. Tongay, J. Wu, Y. Zhang, F. Wang, *Nat. Nanotechnol.* 9 (2014) 682–686.
- [47] C.H. Lee, G.H. Lee, A.M. van der Zande, W. Chen, Y. Li, M. Han, X. Cui, G. Arefe, C. Nuckolls, T.F. Heinz, J. Guo, J. Hone, P. Kim, *Nat. Nanotechnol.* 9 (2014) 676–681.
- [48] X. Zhu, N.R. Monahan, Z. Gong, H. Zhu, K.W. Williams, C.A. Nelson, *J. Am. Chem. Soc.* 137 (2015) 8313–8320.
- [49] J. Park, Y.H. Ahn, C. Ruiz-Vargas, *Nano Lett.* 9 (2009) 1742–1746.
- [50] K. Pi, K.M. McCreary, W. Bao, W. Han, Y.F. Chiang, Y. Li, S.W. Tsai, C.N. Lau, R.K. Kawakami, *Phys. Rev. B* 80 (2009).
- [51] G. Giovannetti, P.A. Khomyakov, G. Brocks, V.M. Karpan, J. van den Brink, P.J. Kelly, *Phys. Rev. Lett.* 101 (2008) 026803.
- [52] H. Hirakawa, S. Shiota, Y. Shiraishi, H. Sakamoto, S. Ichikawa, T. Hirai, *ACS Catal.* 6 (2016) 4976–4982.
- [53] Y. Kofuji, Y. Isobe, Y. Shiraishi, H. Sakamoto, S. Tanaka, S. Ichikawa, T. Hirai, *J. Am. Chem. Soc.* 138 (2016) 10019–10025.
- [54] M.K. Weclawski, M. Jakešová, M. Charyton, N. Demitri, B. Koszarna, K. Oppelt, S. Sariciftci, D.T. Gryko, E.D. Głowacki, *J. Mater. Chem. A* 5 (2017) 20780–20788.
- [55] I. Yamanaka, T. Onizawa, S. Takenaka, K. Otsuka, *Angew. Chem. Int. Ed.* 42 (2003) 3653–3655.
- [56] A. Qaseem, F.Y. Chen, X.Q. Wu, R.L. Johnston, *Catal. Sci. Technol.* 6 (2016) 3317–3340.
- [57] C. Wang, M. Long, B. Tan, L. Zheng, J. Cai, J. Fu, *Electrochim. Acta* 250 (2017) 108–116.
- [58] J. Bandara, I. Guasaquillo, P. Bowen, L. Soare, W.F. Jardim, J. Kiwi, *Langmuir* 21 (2005) 8554–8559.
- [59] Y. Isaka, Y. Yamada, T. Suenobu, T. Nakagawa, S. Fukuzumi, *RSC Adv.* 6 (2016) 42041–42044.